Ocean-Land-Atmosphere Research
A SCIENCE PARTNER JOURNAL

RESEARCH ARTICLE

Increase in Tropospheric Water Vapor Amplifies Global Warming and Climate Change

Vikas Kumar Patel and Jayanarayanan Kuttippurath*

CORAL, Indian Institute of Technology Kharagpur, Kharagpur 721302, India.

*Address correspondence to: jayan@coral.iitkgp.ac.in

Citation: Patel VK, Kuttippurath J. Increase in Tropospheric Water Vapor Amplifies Global Warming and Climate Change. *Ocean-Land-Atmos. Res.* 2023;2:Article 0015. https://doi.org/10.34133/olar.0015

Submitted 28 January 2023
Accepted 12 June 2023
Published 6 July 2023

Among the greenhouse gases (GHGs), atmospheric water vapor is the most abundant, has a large influence on the radiation budget of Earth, and plays a decisive role in regional weather processes. We investigate the long-term (1980–2020) changes in global tropospheric water vapor using satellite, radiosonde, and reanalysis data and assess the impact of changes in water vapor on regional and global climate with respect to its radiative feedback. The annual climatology of global tropospheric water vapor varies from 5 to 60 kg/m^2 across different regions. Except in the tropics, there is a strong seasonal cycle in both the southern and northern hemispheres, with the highest values in summer (25 to 65 kg/m^2) and smallest values in winter (5 to 20 kg/m^2). Most regions show positive trends in the annual mean tropospheric water vapor, at about 0.025 to 0.1 kg/m^2/year, for the period of 1980–2020, with a notable increase in the Arctic because of the high rise in temperature there. Throughout the troposphere (except 200 hPa), the annual mean specific humidity shows significant positive trends over both land and oceans, with the highest values of approximately 0.015 g/kg/year at 1000 hPa in the tropics. The associated radiative effects on shortwaves at the surface vary from −5 to −70 W/m^2, with the highest values at Manaus, Porto, and Hanty–Mawsijsk (tropical stations) and the smallest values of about −5 to −10 W/m^2 in the polar regions. The model projections for future high-emission scenarios show a large increase in atmospheric water vapor, approximately twice the current value in the polar latitudes by the end of the 21st century. This is a great concern for global and regional climate, as the rise in water vapor would further augment global warming and phenomena, such as the Arctic amplification. Therefore, this study cautions that there is a significant rise in tropospheric water vapor across latitudes and altitudes, which could further increase the global temperature and, thus, accelerate global climate change.

Introduction

The troposphere contains approximately 99% of the atmospheric water vapor, which plays a crucial role in Earth's climate system. It is at the center of all major atmospheric processes and plays an essential role in cloud formation. Even in the most extreme weather events, including tropical cyclones and thunderstorms, water vapor is one of the key elements. On the other hand, it is one of the most abundant greenhouse gases (GHGs) and has strong positive feedback on temperature [1–3]. Water vapor controls evapotranspiration processes and is, thus, connected to the global energy budget and hydrological cycle. Therefore, understanding and monitoring atmospheric water vapor changes are critical for assessing climate change and feedback mechanisms in Earth system models.

Several studies have examined the changes in specific humidity and integrated column water vapor in relation to global warming [4–8]. Measurements and model simulations reveal that the water vapor amount is projected to rise as a result of anthropogenic GHG-induced warming [9–11]. Climate model results also suggest that anthropogenic forcing, instead of natural variability, is the primary cause of the increase in atmospheric water vapor [12].

Studies have reported trends in water vapor with respect to different time periods for different regions. For instance, the changes in water vapor in the northern hemisphere were investigated by analyzing radiosonde measurements from 1973 to 1995 [13]. They reported positive trends at most stations, approximately 0.5%/dec. Similarly, Bengtsson et al. [14] estimated the trends in global column water vapor using the European Centre for Medium-Range Weather Forecasts Reanalysis 40 years (ERA40) data from 1979 to 2001. They observed a significant rising trend of approximately 0.36 kg/m^2/dec. The trends in global water vapor estimated using the measurements from the Global Ozone Monitoring Experiment reported approximately 2.8 ± 0.8%/dec for the period of 1996–2002 [2]. Furthermore, the trends in global water vapor using satellite measurements for the period of 1996–2006 were also investigated by Mieruch et al. [15]. They showed that water vapor is increasing significantly in Greenland (4 to 5%/year) and part of Europe (1 to 2%/year), but declining in the Northwest United States (−1 to −2%/year) as well as Amazonia and central Africa (approximately −1%/year).

Because of their tight coupling with atmospheric circulation, simulating and understanding the role of water vapor and clouds in climate are complicated. This coupling also presents a major bottleneck in terms of narrowing the uncertainty of cloud feedback to surface air temperature [16]. The accurate amount of global warming caused by the rise in GHGs in the atmosphere is still under discussion. This uncertainty is mainly due to the difficulty in quantifying the role of the feedback mechanisms

in the climate system, including water vapor. If a specific feedback mechanism plays a significant role in GHG-induced climate change, then it should also play a significant role in natural variability. Using water vapor feedback as an example, assume an internally generated forcing, such as a change in net cloud cover associated with atmospheric instability, inducing a warm anomaly in the surface–troposphere system. A resultant rise in atmospheric water vapor and greenhouse trapping of outgoing radiation would diminish the anomaly's radiative damping of surface air temperature and, hence, a rise in its magnitude. Therefore, although water vapor feedback plays no role in the generation of temperature anomalies, whether externally driven or internally generated, it can have a major effect on their magnitude. In this way, water vapor feedback can "enhance" or "amplify" surface–troposphere temperature anomalies. Even though water vapor feedback is important to the sensitivity and variability in climate [17,18], it is challenging to obtain an overall understanding of its impact on climate. For instance, there is still uncertainty in understanding whether water vapor feedback amplifies externally imposed climate changes, such as those caused by the rise in GHGs, to the same extent as it amplifies internally generated climate variations.

Therefore, to acquire detailed knowledge of Earth's climate system and how it responds to rising GHG concentrations, it is essential to examine the variability and changes in water vapor over recent decades across latitudes. Here, we examine the variability and long-term changes (1980–2020) in global tropospheric water vapor using measurements and reanalysis data, analyze the factors affecting the variability and trends in water vapor, and quantify the impact of changes in water vapor on temperature by estimating its radiative effects.

Materials and Methods

Data

Specific humidity from satellite, radiosonde, reanalysis, and CMIP6

The ERA5 monthly averaged specific humidity profile is considered from the surface to the tropopause for the period of 1980–2020. ERA5 is the recent climate reanalysis produced by the European Center for Medium-Range Weather Forecasts [19]. In addition, specific humidity from Atmospheric Infrared Sounder (AIRS) satellite observations is also considered. AIRS provides the mixing ratio at different pressure levels in the atmosphere, and therefore, the specific humidity is calculated by employing the formula $q = w/(1 + w)$, where w stands for the mixing ratio and q is the specific humidity. AIRS water vapor retrievals have been used in several previous studies, including feedback analysis, climate model validation, and weather forecasting [20,21]. We also use the integrated global radiosonde archive version 2 (IGRA-2) monthly tropospheric radiosonde vapor pressure profiles (1,000 to 100 hPa) [22]. Considering that vapor pressure is measured using radiosondes, we use the following formula to compute specific humidity:

$$q = -0.622\frac{e}{p - 0.379e} \quad (1)$$

where q (kg kg^{-1}) represents specific humidity, and e and p represent the vapor pressure and air pressure in hectopascal, respectively. To determine the tropospheric column water vapor (TCWV), we vertically integrate the specific humidity measurements from each station. Further information about the datasets is given in Table.

To understand the future changes in water vapor, monthly mean near-surface specific humidity is used from Coupled Model Intercomparison Project Phase 6 (CMIP6) models, Community Integrated Earth System Model (CIESM), and CNRM-CM6-1HR, under the scenarios Shared Socioeconomic Pathways 126 (SSP126), SSP245, and SSP585 for the period of 2015–2100.

Auxiliary data

Wind transport and evapotranspiration are the primary water vapor sources over land. Here, the monthly mean soil moisture and evapotranspiration are obtained from the Global Land Data Assimilation System (GLDAS) and Famine Early Warning Systems Network Land Data Assimilation System, respectively; evaporation (CNRM-CM6-1HR) and sea surface temperature (SST) are obtained from ERA5; and surface air temperature over land is obtained from the climatic research unit (CRU) for the period of 1980–2020. A detailed description of the data is given in Table.

To examine the influence of different atmospheric and oceanic processes on water vapor distribution, we have considered the following data or indices to represent the respective process in causal analyses. These are the solar flux (SF) and northern/southern hemisphere sea ice extent (NHSIE/SHSIE), Antarctic Oscillation (AAO), Oceanic Nina Index (ONI) for El Niño Southern Oscillation (ENSO), Quasi-Biennial Oscillation (QBO), Pacific Decadal Oscillation (PDO), Northern Atlantic Oscillation (NAO), and Arctic Oscillation (AO). These data are publicly available from the National Oceanic and Atmospheric Administration Climate Prediction Center (NOAA CPC).

Methodology

Computation of TCWV

TCWV is calculated by the vertical integration of specific humidity (derived from ERA5 and AIRS) from the surface to 100 hPa using the following equation:

$$\mathrm{TCWV} = -\frac{1}{g}\int_{p_s}^{p_o} q\,dp \approx -\frac{1}{g}\sum_{p_s}^{p^o} q_i\,\Delta p \quad (2)$$

where p_o and p_s are the air pressure at the top of the troposphere (100 hPa) and surface air pressure in hectopascal, respectively; i is the air pressure level; g (9.8 m s^{-2}) represents gravitational acceleration; p in hectopascal is the air pressure; and q represent the specific humidity.

The AIRS TCWV data are used to assess the accuracy of ERA5. In this case, statistical measures, such as the mean bias error (MBE) and root mean square error (RMSE), are employed. The following formulae are used:

$$\mathrm{RMSE} = \sqrt{\frac{\sum_{i=1}^{N}\left(\mathrm{TCWV}_{Ri} - \mathrm{TCWV}_{Ai}\right)^2}{N}} \quad (3)$$

$$\mathrm{MBE} = \frac{\sum_{i=1}^{N}\left(\mathrm{TCWV}_{Ri} - \mathrm{TCWV}_{Ai}\right)}{N} \quad (4)$$

where TCWV_{Ri} and TCWV_{Ai} are the TCWV derived from reanalysis data and AIRS measurements, respectively, and N represents the total number of observations.

Table. Description of datasets used in this study.

Variables	Spatial resolution	Data source	Time period
Specific humidity/mixing ratio profile	0.25° × 0.25°	ERA5	1980–2020
	1° × 1°	AIRS	2003–2020
Vapor presure		Radiosonde (IGRA-2)	1980–2020
Water vapor flux	0.5° × 0.625°	MERRA-2	1980–2020
Surface air temperature	0.5° × 0.5°	CRU	1980–2020
Sea surface temperature	0.25° × 0.25°	ERA5	1980–2020
Evaporation (ocean)	0.25° × 0.25°/0.5° × 0.5°	ERA5/CNRM-CM6-1HR	1980–2014
Evapotranspiration (land)	0.1°× 0.1°	FLDAS	1980–2020
Soil moisture	0.25° × 0.25°	GLDAS	1980–2020
Precipitation	0.25° × 0.25°	GPCC/ERA5	1980–2020
Atmopsheric–oceanic circulation data		NOAA CPC	1980–2020
1.AAO			
2.NAO			
3.AO			
4.QBO			
5.PDO			
6.ONI			
Solar flux		NOAA CPC	1980–2020
NHSIE		NOAA CPC	1980–2020
SHSIE		NOAA CPC	1980–2020
Future projection			
Specific humidity		CNRM-CM6-1HR	1980–2100
		CIESM	1980–2100

AAO, Antarctic Oscillation; AO, Arctic Oscillation; QBO, Quasi-Biennial Oscillation; NAO, North Atlantic Oscillation; PDO, Pacific Decadal Oscillation; ONI, Oceanic Niña Index; NHSIE, northern hemisphere sea ice extent; SHSIE, southern hemisphere sea ice extent

We observe that the bias in ERA5 compared to AIRS is very small in both polar and midlatitude regions (Fig. S1). However, in tropical regions, such as the Intertropical Convergence Zone (ITCZ) and Amazonia, ERA5 overestimates AIRS by approximately 4 to 5 kg/m^2. Furthermore, in Southeast Asia, East China, and United States, ERA5 overestimates AIRS by 3 to 5 kg/m^2. The RMSE computed for the regions ITCZ, northeast India, Amazonia, and Indo-Pacific warm pool is approximately 3 to 6 kg/m^2. We have also averaged the MBE and RMSE globally, land and oceans, tropics, northern midlatitude (NML), southern midlatitude (SML), Arctic, and Antarctica. The bias in ERA5 is relatively large in the tropics (with MBE of 1.8 to 2 kg/m^2 and RMSE of 2.4 to 2.6 kg/m^2) and very small in Antarctica (both MBE and RMSE are approximately 0.3 to 0.4 kg/m^2). The bias in global land regions is also small (approximately 1 kg/m^2) and it is comparable to that in the Arctic. In comparison to the global land regions, the bias in the global ocean (MBE of 1.2 to 1.4 kg/m^2 and RMSE of 1.4 to 1.5 kg/m^2) is slightly higher. A similar bias is also observed by Patel and Kuttippurath [23] in the Indian subcontinent, where ERA5 overestimates AIRS, mainly because of summer monsoon clouds, when AIRS cannot capture the entire column of water vapor through clouds. In addition, similar biases in the AIRS data were also shown by previous studies [24,25]. Lower water vapor is measured by AIRS during the monsoon season, suggesting that the retrieval is limited by initial guess values, and cloud clearing could also exacerbate this. Further analyses are carried out on the basis of the ERA5 data due to its availability for a longer period, and these data show comparable results with satellite measurements.

Estimation of distribution, variability, and trends in water vapor

Monthly averaged TCWV is used to analyze the annual and seasonal climatology for the period of 1980–2020. Seasons in the northern hemisphere are defined as winter (December–January–February, DJF), spring (March–April–May, MAM),

summer (June–July–August, JJA), and autumn (September–October–November, SON). However, it is reversed for the southern hemisphere, i.e., JJA is winter, SON is spring, DJF is summer, and MAM is autumn. Interannual variability in TCWV is examined for various regions, including global land and oceans, tropics (23°26′10.8″N to 23°26′10.8″S), NML (30° to 60°N), SML (30° to 60°S), Arctic, and Antarctic, for the period of 1980–2020. The trend in water vapor is determined using linear regression with the uncertainty computed at the 95% confidence interval (CI).

Trends in surface air temperature, SST, evaporation, evapotranspiration. and soil moisture are also calculated to understand their relation to the changes in water vapor. The vertical distribution and trends in specific humidity in the troposphere (1,000 to 100 hPa) are also estimated for all regions. Multiple linear regression (MLR), rotated principal component analysis (RPCA), and Granger causality test are carried out to examine the influence of different local and global drivers of atmospheric water vapor changes. The methodology for MLR and RPCA is discussed in the Supplementary Materials.

Granger causality

To gain an understanding of the causative relationship between drivers and water vapor in each region, we carry out the Granger causality test. Granger causality occurs when all relevant information except the current value of $x(t)$ improves the capacity to predict possible $y(t)$, and variable $x(t)$ Granger causes $y(t)$. A "feedback" relationship between a cause and its effect is established when both the cause and the effect are capable of Granger causation. To be more exact, the test is specified in terms of the linear relationships that exist between $x(t)$ and the lagged time series $x(t-\tau)$ and $y(t-\tau)$, with lags that range from 1 to the maximum value $\tau_{\max}$. Granger proposed a bivariate model consisting of 2 stationary time series in the aim of causal analysis ($x(t)$ and $y(t)$).

$$y(t) = \sum_{\tau=1}^{\tau_{\max}} \alpha_\tau y(t-\tau) + \sum_{\tau=1}^{\tau_{\max}} \beta_\tau x(t-\tau) + \varepsilon_t \quad (5)$$

$$x(t) = \sum_{\tau=1}^{\tau_{\max}} \alpha_\tau x(t-\tau) + \sum_{\tau=1}^{\tau_{\max}} \beta_\tau y(t-\tau) + \delta_t \quad (6)$$

where $x(t)$, $y(t)$ represents stationary time series; ε_t, δ_t represents white noise; the coefficients are α_τ and β_τ; and $\beta_\tau \neq 0$, for $x(t)$ is stated for Granger causing $y(t)$.

The following procedure is used to perform the Granger causality. First, time series stationarity is evaluated using a nonparametric test. The difference is used if the time series is nonstationary, and vector autoregressive models are built. Second, for each region, vector autoregressive models are created between "response ($y(t)$)," i.e., water vapor, and "cause ($x(t)$)," i.e., each index or drivers, independently. Finally, to assess the null hypothesis (Ho: $x(t)$ does not Granger cause $y(t)$), a Granger causality test is used. To explain the temporal lag in Granger causality, each variable is given a maximum allowable lag ($\tau_{\max}$) of 5 months.

To study the strength of the teleconnection between drivers and water vapor in different regions, conditional cross-correlation is used. It is also called the lagged correlation method and is commonly used in climate science to examine the relation between 2 processes [26]. This methodology is based on the Pearson correlation between the time series $x(t)$ and $y(t)$ at certain lags τ. Here, we apply this approach to find the correlation across all the lags by defining the $\tau_{\max}$ and then compute the correlation (ρ_τ) across the lags:

$$C_{\tau_{\max}} = \max\{\pi | \rho_\tau(x(t), y(t+\tau))| : 0 \leq \tau \leq \tau_{\max}\} \quad (7)$$

Water vapor and temperature relationship

Water vapor and temperature are connected by a positive feedback mechanism in the troposphere. Therefore, we analyze the water vapor–temperature relation in 2 steps: (a) analyze the impact of surface temperature on water vapor and (b) assess the influence of increasing water vapor on surface temperature through water vapor radiative effects (WVRE). The water vapor change per degree Celsius rise in surface temperature is computed by using the relation ΔTCWV (%)/ΔT, where T is the surface temperature. Furthermore, under clear sky conditions, the WVRE on SW (shortwave) irradiances at the surface are simulated using Santa Barbara's Discrete Ordinates Radiative Transfer (DISORT) model with 4 streams [27]. It is a model that estimates plane-parallel radiative transfer under both clear sky and cloudy conditions at the surface and within the atmosphere, which includes all processes that affect the infrared and visible radiation fields. This model is based on the complex DISORT module, low-resolution atmospheric transmission models, and Mie scattering principle. Here, we assume that irrespective of the solar zenith angle, the angular distribution of surface reflected radiation is completely isotropic. Given the dearth of angular reflection data, this Lambertian reflection assumption is probably suitable in most instances. The DISORT algorithm utilizes a flat Earth coordinate system. This assumption is generally true when the region of interest has a vertical extent that is significantly smaller than the radius of Earth. When dealing with common causes of scattering in Earth's atmosphere, this is the typical outcome in most cases. Gas absorption, on the other hand, can be a relevant factor even at very high elevations (e.g., ultraviolet absorption by stratospheric ozone). When high sun zenith angles are considered, the assumption of flat Earth could potentially lead to considerable errors [23,27,28]. Measurements from 33 radiosonde stations that represent different regions of the world are considered in this calculation (Fig. S2 and Table S1).

To estimate the change in the WVRE because of water vapor rise, the WVRE in the third (higher 75%) [Q3] and first (lower 25%) [Q1] quartiles are estimated by arranging water vapor data in ascending order. To understand the rise in water vapor and associated changes in the WVRE, the quartile difference [Q3 − Q1] is computed. In the percentage of steps, spanning from 0.001 to 0.02 μm, the SW wavelength range is considered to be 0.25 to 4.0 μm. The simulation begins with a step size of 0.005 μm at 0.25 μm and increases to 4 μm. For more information on the WVRE estimations in SW, refer to Patel and Kuttippurath [23] and Vaquero-Martínez et al. [28]. To account for the atmospheric state, the model is fed with water vapor and ozone profiles at each radiosonde station. Because thermal radiation is hardly detectable in the wavelength range under consideration, it is not taken into account in these calculations. The model is run twice, first with all data (including trace gases and other GHGs) and second with all data excluding water vapor (which is set to zero). Thus, the WVRE can be estimated as the difference in net irradiance (downward minus upward) at the surface simulated with and without water vapor.

$$\text{WVRE} = \left(I^{\downarrow}_{\text{TCWV}} - I^{\uparrow}_{\text{TCWV}}\right) - \left(I^{\downarrow}_{\text{dry}} - I^{\uparrow}_{\text{dry}}\right) \quad (8)$$

where $I^{\downarrow}_{TCWV}$ and $I^{\uparrow}_{TCWV}$ are the downward and upward irradiance with TCWV, respectively; $I^{\downarrow}_{dry}$ (downward) and $I^{\uparrow}_{dry}$ (upward) represent irradiance with no TCWV.

Results and Discussion

The distribution of global tropospheric water vapor

Figure 1 illustrates the annual and seasonal climatology of global tropospheric water vapor derived from ERA5. Figure S3 illustrates the analysis of its variability based on standard deviation (SD). The global annual mean water vapor varies from 5 to 60 kg/m^2 across the regions. Very high values (50 to 55 kg/m^2) are observed over the tropical oceans, primarily in the east and west central Pacific and eastern Indian Ocean. Similar water vapor amounts are also observed in tropical land regions. For example, approximately 45 to 55 kg/m^2 of water vapor is observed in Central Africa, Southeast Asia, and Amazonia. The higher temperatures and solar radiation throughout the year in the tropics cause high evaporation, which lead to high amount of water vapor there. In contrast, a small amount of water vapor is found in the polar regions (both Arctic, including Greenland and Antarctic) and regions with high elevation (e.g., Tibetan Plateau), approximately 5 kg/m^2, primarily because of the low temperature there. Figure S3 depicts larger variability in water vapor observed in parts of the Pacific and Indian Oceans, with an annual mean SD of 3 to 4 kg/m^2.

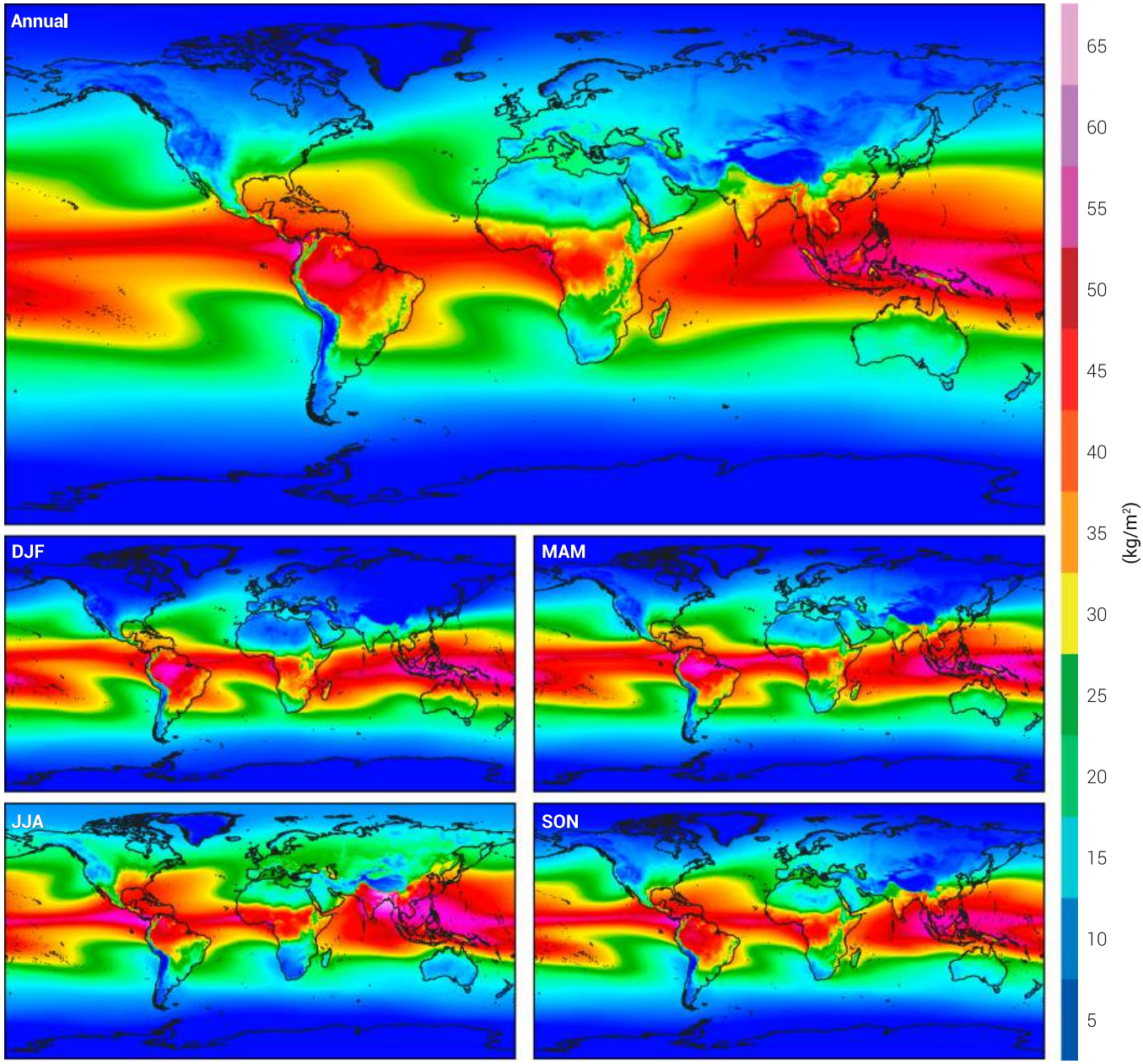

Fig. 1. Distribution of annual and seasonal (e.g., winter [DJF], spring [MAM], summer [JJA], and autumn [SON] for the northern hemisphere) water vapor derived from ERA5 for the period 1980–2020.

There is a strong seasonal variability in global water vapor distribution, as shown in Fig. 1, with very high amounts in summer and lowest amounts in winter, except in the tropics, where water vapor is high throughout the year. In general, there is a gradual increase in water vapor from winter (5 to 15 kg/m^2) to summer (15 to 65 kg/m^2), except in the tropics. The small amount of water vapor in winter is mainly due to the dry continental winds and relatively lower temperature. It gradually increases and shows slightly higher values in spring than in winter because of enhanced thermal heating and associated evaporation/evapotranspiration. As mentioned above, high amounts of water vapor are observed in summer, with very high values in the Indian subcontinent, Southeast Asia, Amazonia, Central Africa, ITCZ, Bay of Bengal, north Atlantic Ocean, Arabian Sea, northern Indian Ocean, and eastern United States, about 30 to 65 kg/m^2. These high values of water vapor over the Indian subcontinent are mainly due to moisture transport by winds from the Arabian Sea and Indian Ocean (Fig. S4). Similarly, the high variability in the Indian subcontinent, with an SD of 4 to 8 kg/m^2, is due to large variability in precipitation across the seasons driven by the monsoon climate (Fig. S5). Because of the very dry atmosphere, water vapor variability is very small (SD < 2 kg/m^2) in the Antarctic, Arctic, desert, and high terrain regions.

Interannual variability

Interannual variability in the annual mean water vapor, surface air temperature, and SST over global land, global ocean, tropics, NML, SML, and Arctic are analyzed for the period of 1980–2020 and are illustrated in Fig. 2. In addition, variability in evapotranspiration (land) and evaporation (ocean) are also investigated for these regions (Fig. S6). Water vapor gradually increased from 1995 onward in all regions. A peak in water vapor is observed in 1997–1998 in all regions, which is connected to the strong El Niño event during the period (Fig. S7). The drop during 1991–1992 is the result of the Mount Pinatubo volcanic eruption [29]. Volcanic aerosols impeded solar heating and, thus, caused global cooling and inflicted a 0.5 kg/m^2 decrease in global water vapor [30]. A gradual increase in temperature and SST has also been observed in all regions since 1995. For example, the variability in water vapor is consistent with that in surface air temperature over land and SST of the oceans. In addition, evapotranspiration and evaporation in land and ocean, respectively, show a gradual enhancement from 1995 onward, which is consistent with

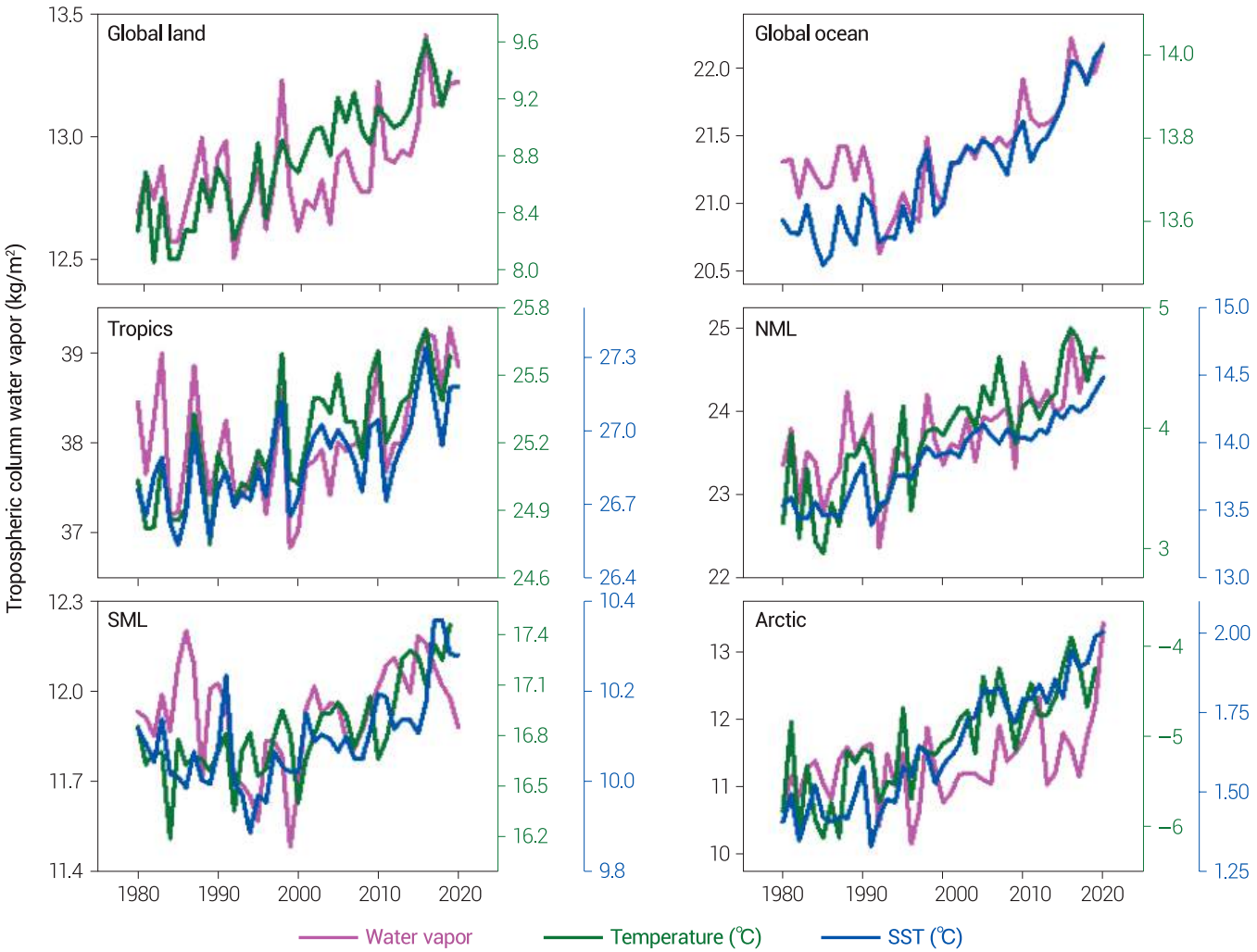

Fig. 2. Temporal evolution of water vapor, surface air temperature, and sea surface temperature (SST) averaged over global land, global ocean, tropics (23.43°N to 23.43°S), northern midlatitudes (NML) (23.43°N to 66.55°N), southern midlatitudes (SML) (23.43°S to 66.55°S), and Arctic (66.55°N to 90°N).

the water vapor changes in the respective regions. There are very high values, particularly in the tropical ocean and SML, before 1990. Before this, there were only a few global observations of water vapor available, and therefore, the high water vapor in these regions before 1990 may be due to the associated uncertainties in the model simulations [31].

To understand the variability caused by atmospheric–oceanic processes, SF and sea ice on water vapor, Granger causality, MLR, and RPCA analyses are carried out for the tropics, NML, SML, Arctic, and Antarctic. Granger causality reveals that AAO, ONI, PDO, NHSIE, and SHSIE significantly influence the variability in water vapor in the tropics with lags of 2, 1, 1, 1, and 1 month, respectively, consistent with the MLR analyses, where the contribution of NAO is 13.02%, PDO is 16.15%, NHSIE is 14.74%, ONI is 29.39%, and SHSIE is 7.80% (Fig. 3 and Table S2). The RPCA (Fig. S8) also exhibits similar variability in the tropics, with a strong correlation to PDO (0.81) and ONI (0.83). Similarly, AO (13.95%), NAO (18.94%), NHSIE (24.34%), and PDO (24.65%) modify the water vapor variability in the Arctic, as analyzed from the MLR, but the impacts of AO and NAO are absent in the Granger causality (PDO is present with a lag of 1 month). Furthermore, PDO (22.54%), NHSIE (23.86%), NAO (18.21%), and AO (16.24%) influence water vapor variability in the NML, as revealed by MLR and by Granger causality with a lag of 1 month. The PDO is a long-term change in SST between the northern and southern Pacific. In general, these SST changes switch between the north and south Pacific every 20 to 30 years (e.g., warm and cold phases). As our analysis focuses on the previous 4 decades, we can observe one complete PDO cycle (1980–2000 warm phase; see Fig. S4), which can be used to understand the impact of PDO on the variability in water vapor. PDO affects the variability in water vapor directly by modifying SST and atmospheric circulation and indirectly by modifying ENSO. The ENSO impact is high during the cold PDO phase [30]. However, the physical mechanism of PDO is still not fully understood [32]. There is a significant contribution of AAO to the water vapor variability in the SML and Antarctica regions. Most importantly, NHSIE highly affects water vapor in the Arctic with a negative lag correlation of −0.6, which is also demonstrated in another study [33]. Likewise, SHSIE influences the water vapor distribution in SML and Antarctica.

Trends in water vapor

Trends in column water vapor

The distribution of seasonal and annual mean column water vapor trends and their statistical significance at the 95% CI are illustrated in Fig. 4. Significant positive trends are estimated in the Indian subcontinent, Arabian Sea, Bay of Bengal, eastern Pacific Ocean, Southeast Asia, and Australia, at about 0.05 to 0.1 kg/m^2/year. Slightly smaller positive trends are found in Amazonia, northern Africa, and the northern Atlantic Ocean, at about 0.025 to 0.05 kg/m^2/year. In the northern hemisphere, water vapor is increasing at a stronger rate than that in the southern hemisphere. For example, the Arctic shows high positive trends (approximately 0.025 kg/m^2/year), whereas Antarctica exhibits no significant trend. In contrast, there is a negative trend in Central Africa, in the northwest United States, in regions in South America, and in some areas in the Pacific Ocean. Our finding is consistent with that of Mieruch et al. [15], in which they reported positive trends in water vapor across the northern hemisphere (0.02 to 0.04 kg/m^2/year) but negative trends in the northwestern United States and central Africa, at about −0.02 to −0.04 kg/m^2/year, despite the differences in values due to their different temporal coverages. Water vapor trends are also averaged globally for various time periods, such as 1980–1990, 1990–2000, 2000–2010, and 2010–2020 (Table S3). During 1980–1990, the annual mean trends are insignificant in all regions, except in the Arctic, where trends are positive (approximately 0.07 kg/m^2/year) and statistically significant. Trends estimated for all regions are negative and significant during 1990–2000, except in global land, global ocean (0.03 kg/m^2/year), and NML (0.28 kg/m^2/year), where positive trends are observed. In all regions (except SML and NML) and in the global average, the rate of positive trends in water vapor in the last decade (2010–2020) is higher than that in the previous decade (2000–2010) [0.054 kg/m^2/year for 2010–2020 and 0.04 kg/m^2/year for 2000–2010]. Furthermore, the tropics [0.112 kg/m^2/year for 2010–2020 and −0.05 kg/m^2/year for 1990–2000]

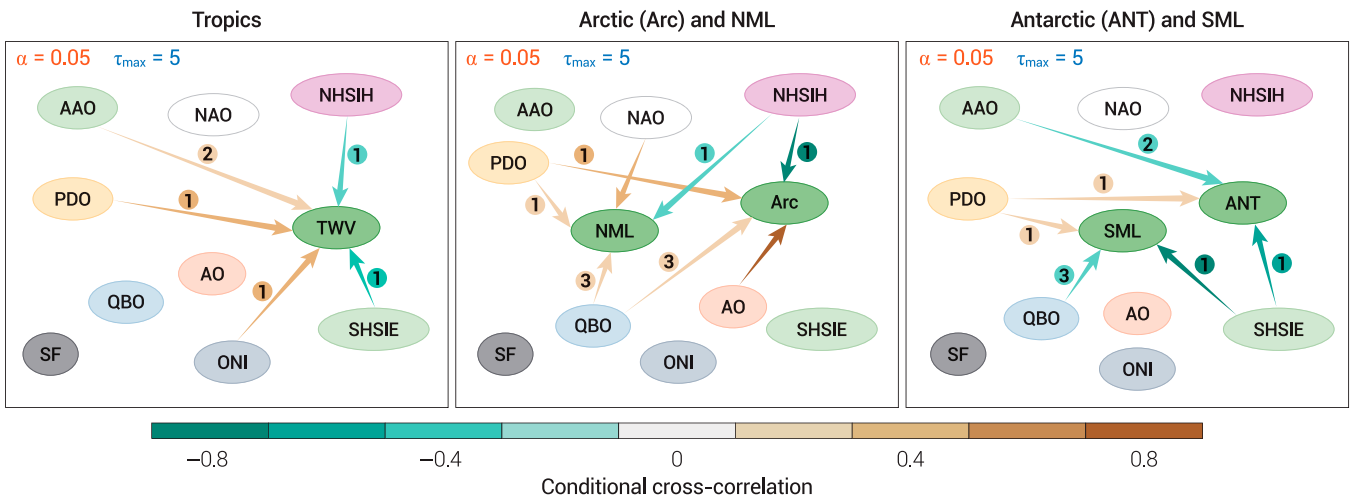

Fig. 3. Influence of global atmospheric and oceanic processes, sea ice extent, and solar flux (SF) on the variability of water vapor over the tropics (TWV), southern midlatitude (SML), northern midlatitude (NML), Arctic (Arc), and Antarctic (ANT) using Granger causality test with statistical significance at 95% CI with a maximum allowable lag of 5 months. Color of the arrow represents the conditional cross-correlation.

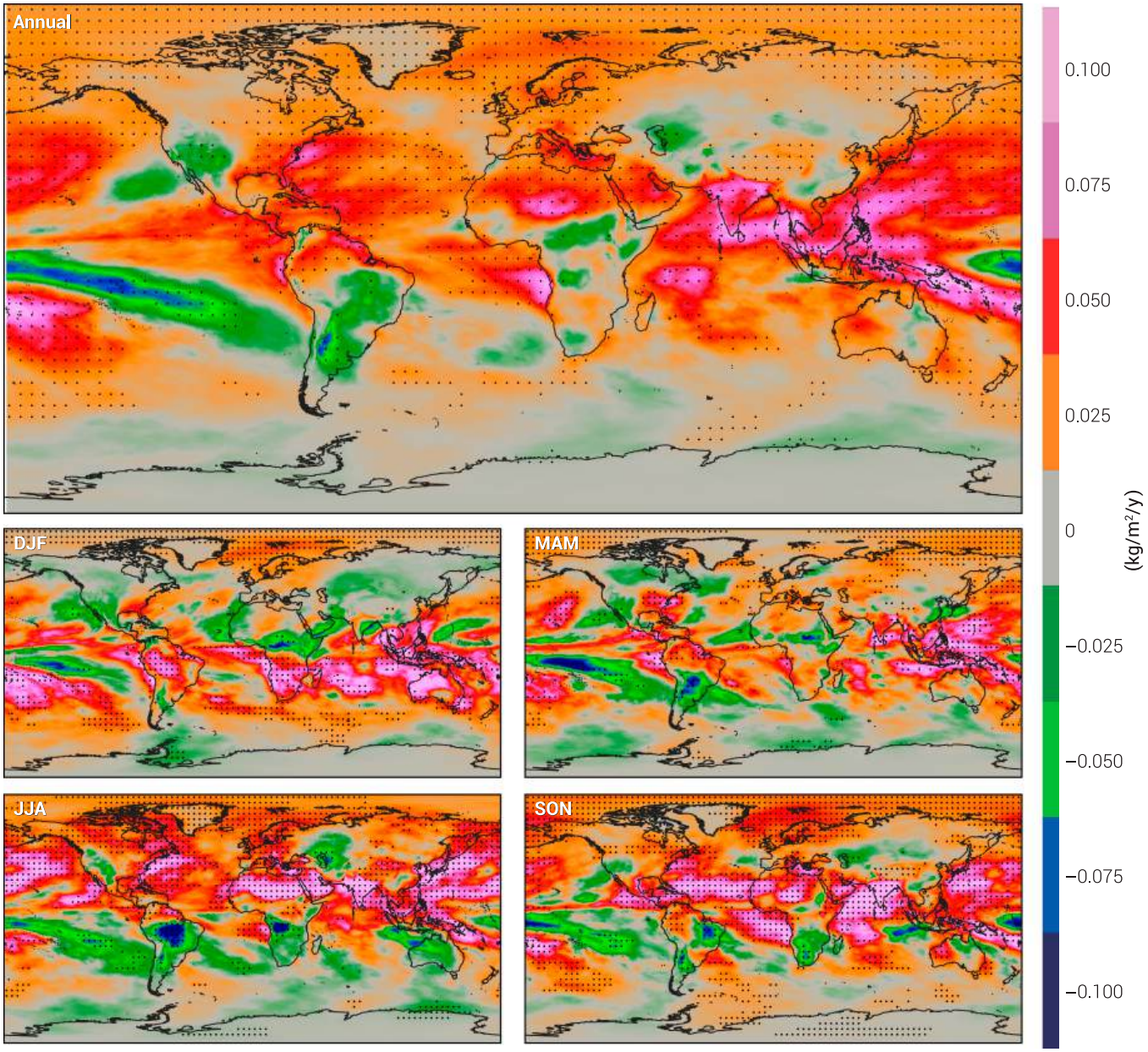

Fig. 4. Distribution of annual and seasonal (e.g., winter [DJF], spring [MAM], summer [JJA], and autumn [SON] for the northern hemisphere) water vapor trends derived from ERA5 for the period 1980–2020. Hatched regions indicate the statistical significance at the 95% CI.

and Arctic [0.09 kg/m^2/year for 2010–2020 and −0.033 kg/m^2/year for 1990–2000] have experienced higher positive trends in recent decades than other regions. Trend values are relatively higher in all regions, except in the midlatitudes over the last decade (2010–2020). This can be the result of a rapid rise in temperature driven by anthropogenic activities.

The trends in water vapor show significant seasonal variation. For example, most regions in the northern hemisphere show noticeable positive trends during summer, at about 0.025 to 0.1 kg/m^2/year, with very high values in the Indian subcontinent, northern Africa (Sahara Desert), northern Pacific Ocean, parts of Asia (Arabian Desert), and northern Atlantic Ocean. Furthermore, positive trends are also observed in the Arctic, approximately 0.025 kg/m^2/year. Our result is in line with the findings of Zhang et al. [34] and Kopec et al. [35], who found that rising SST and moisture transport from the midlatitudes led to an increase in water vapor in the Arctic. During summer in the southern hemisphere, the highest trends are found in the southern Indian Ocean, Australia, southern Africa, Amazonia, and southern Pacific Ocean, at about 0.05 to 0.1 kg/m^2/year. The trends are either zero or negative in winter in most northern hemisphere land regions, except in Europe and the eastern United States, where the trends are insignificantly positive. However, most regions in the southern hemisphere in winter show negative trends, with higher values of −0.05 to −0.1 kg/m^2/year in central South America, central Africa, western Pacific Ocean, and Australia. The trends in autumn are positive and slightly higher in the tropics. For instance, positive trends of 0.075 to 0.1 kg/m^2/year are found over the Indian subcontinent, Arabian Sea, northern Indian Ocean, North Africa, equatorial

Atlantic, and western Pacific. Furthermore, positive trends of 0.025 to 0.05 kg/m^2/year are also found during autumn in the Arctic, but either neutral or small positive trends are observed in the regions close to Antarctica. Conversely, negative trends (−0.05 to −0.075 kg/m^2/year) are estimated in the eastern central Pacific Ocean, Brazil, and southern Africa in autumn. In spring, very high values of 0.025 to 0.1 kg/m^2/year are estimated in the western Pacific Ocean. Slightly lower but positive trends of 0.025 to 0.05 kg/m^2/year are computed over India, Amazon, and eastern United States. Conversely, South America, central Africa, and east central Pacific Ocean show negative trends.

Water vapor distribution and trends in the troposphere

Figure 5 (top) illustrates the vertical profile (up to 100 hPa) of water vapor based on specific humidity (hereafter water vapor) derived from ERA5 averaged for various regions in different seasons. In general, specific humidity decreases significantly with altitude, with the highest values of 10 to 16 g/kg (globally averaged) observed at the surface and the lowest at 100 hPa, approximately 1 g/kg. The annually averaged data at the surface show values of 14 to 17 g/kg in the tropics, which decrease to 5 to 10 g/kg in both SML and NML, and the smallest values (<4.5 g/kg) are found in the polar regions. In the tropics, the specific humidity varies from 2 to 7 g/kg in 800 to 600 hPa altitudes, whereas it is smaller than 5 g/kg in other regions, such as NML, SML, and both polar regions. Furthermore, it varies in all regions above 400 hPa from near 0 to 1.5 g/kg.

The specific humidity profiles show the highest values in summer and smallest values in winter, depending on the region. The seasonal changes in the tropics are very small but pronounced in the altitude range of surface to 500 hPa, where the difference from summer to winter is less than 7 g/kg at the surface, 2 g/kg at 600 hPa, and less than 1.5 g/kg at 500 hPa and above. The difference between summer and other seasons is almost half, e.g., 1.5 to 3 g/kg at the surface for spring and autumn or in the annual mean at all altitudes. Very small seasonal variability is observed in the tropics, and it is comparable with the globally averaged specific humidity values.

We have also estimated the specific humidity trend in these regions for the period 1980–2020 throughout the troposphere, as depicted in Fig. 5 (bottom). The vertical structure of the globally averaged annual mean trends in specific humidity shows the highest values (0.015 g/kg/year) at the surface and rapidly decreases with altitude, and the values are very small or almost zero at 100 hPa. A global increase in specific humidity is also observed at the surface by Dai [7] and Willett et al. [12]. Among the seasons, JJA and SON show the highest trends, particularly below 800 hPa, with values < 0.013 g/kg/year, and they decrease with altitude to nearly zero at 100 hPa. Furthermore, negative

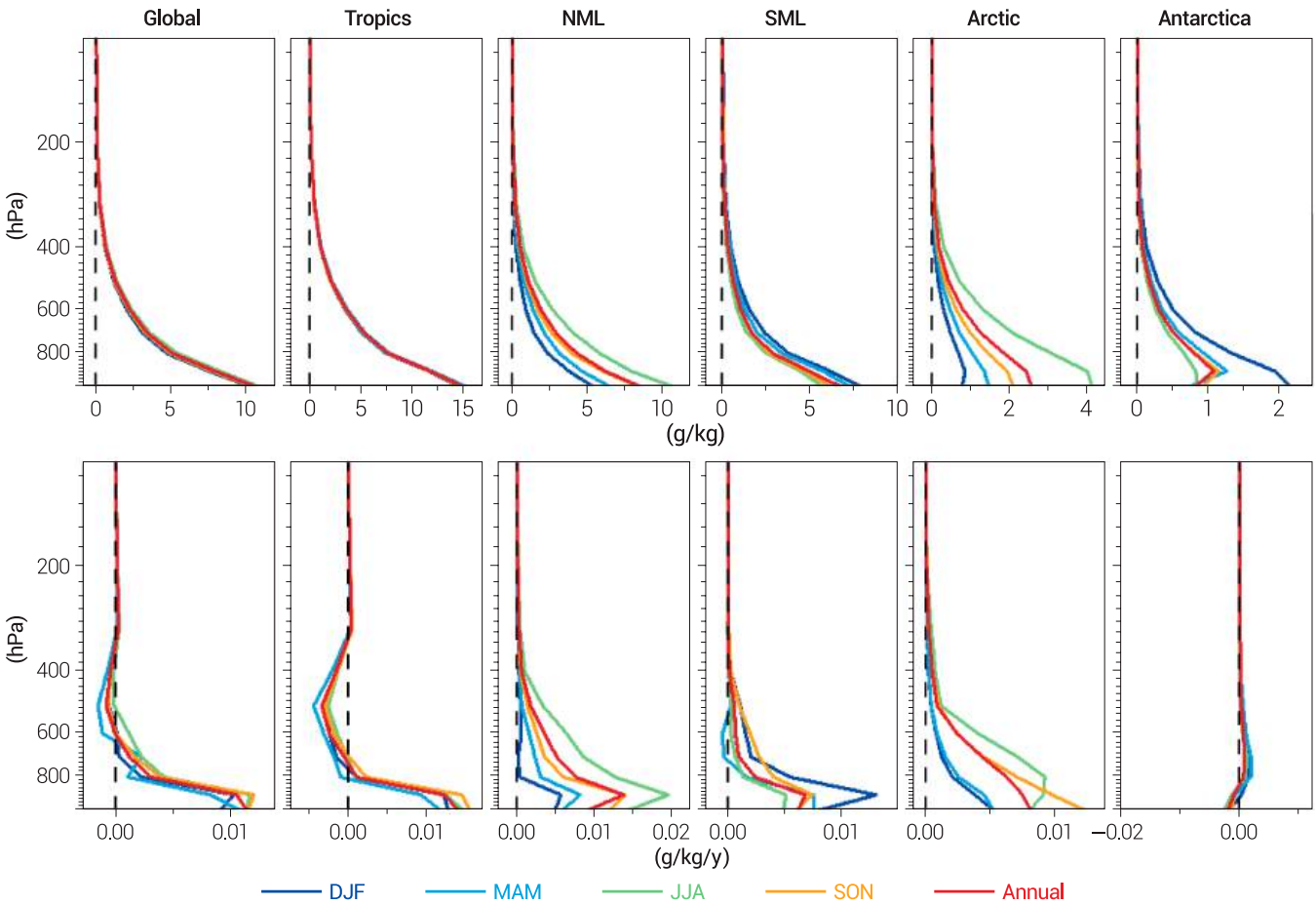

Fig. 5. Vertical distribution of specific humidity (top) and its trend (bottom) in the troposphere averaged over different regions for the period 1980–2020. NML and SML indicate northern and southern midlatitudes, respectively.

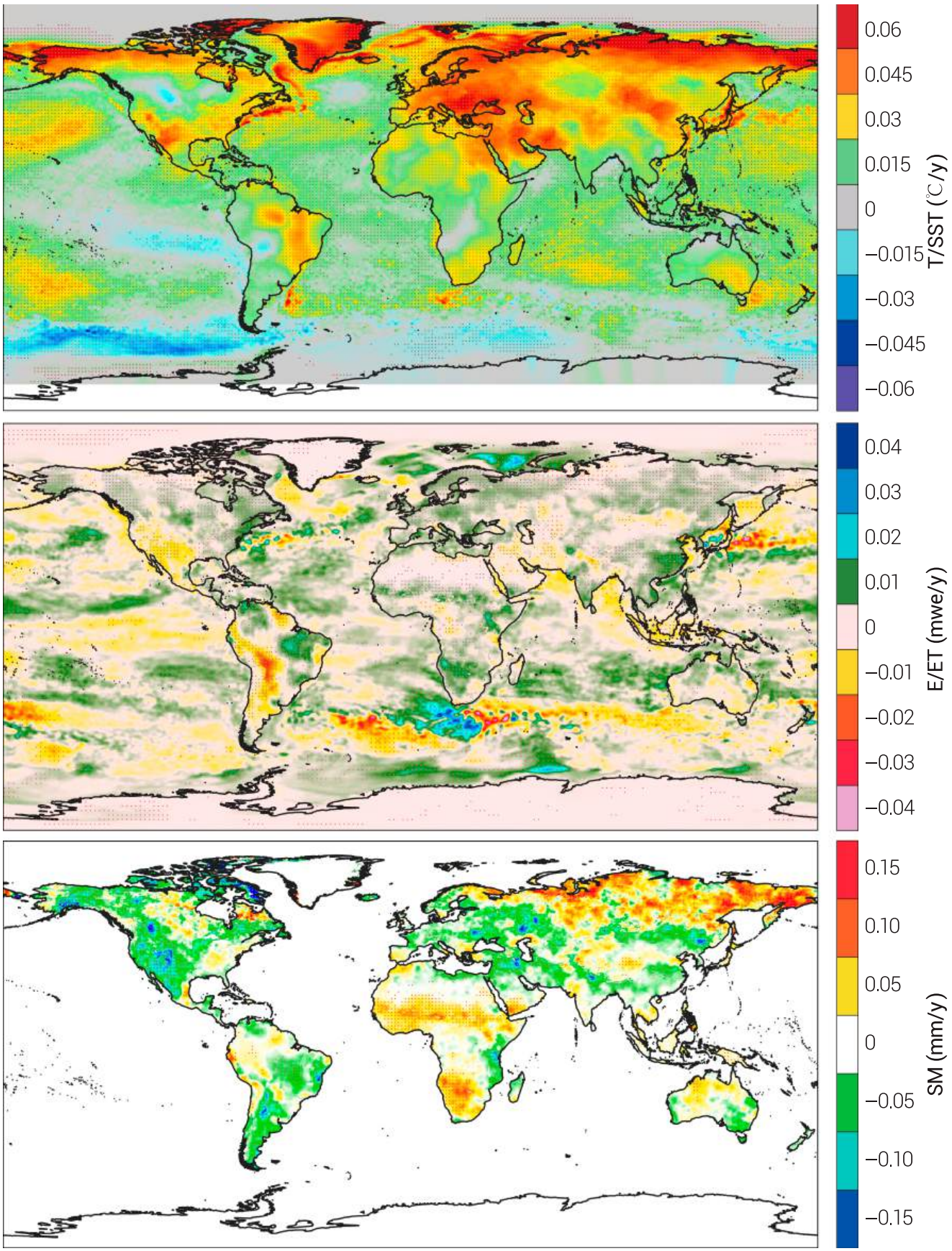

Fig. 6. Distribution of the annual mean surface air temperature (T; land), SST (ocean), evaporation (E; ocean), evapotranspiration (ET; land), and soil moisture (SM) trends for the period 1980–2020. The dotted region indicates the significance of trend at 95% CI.

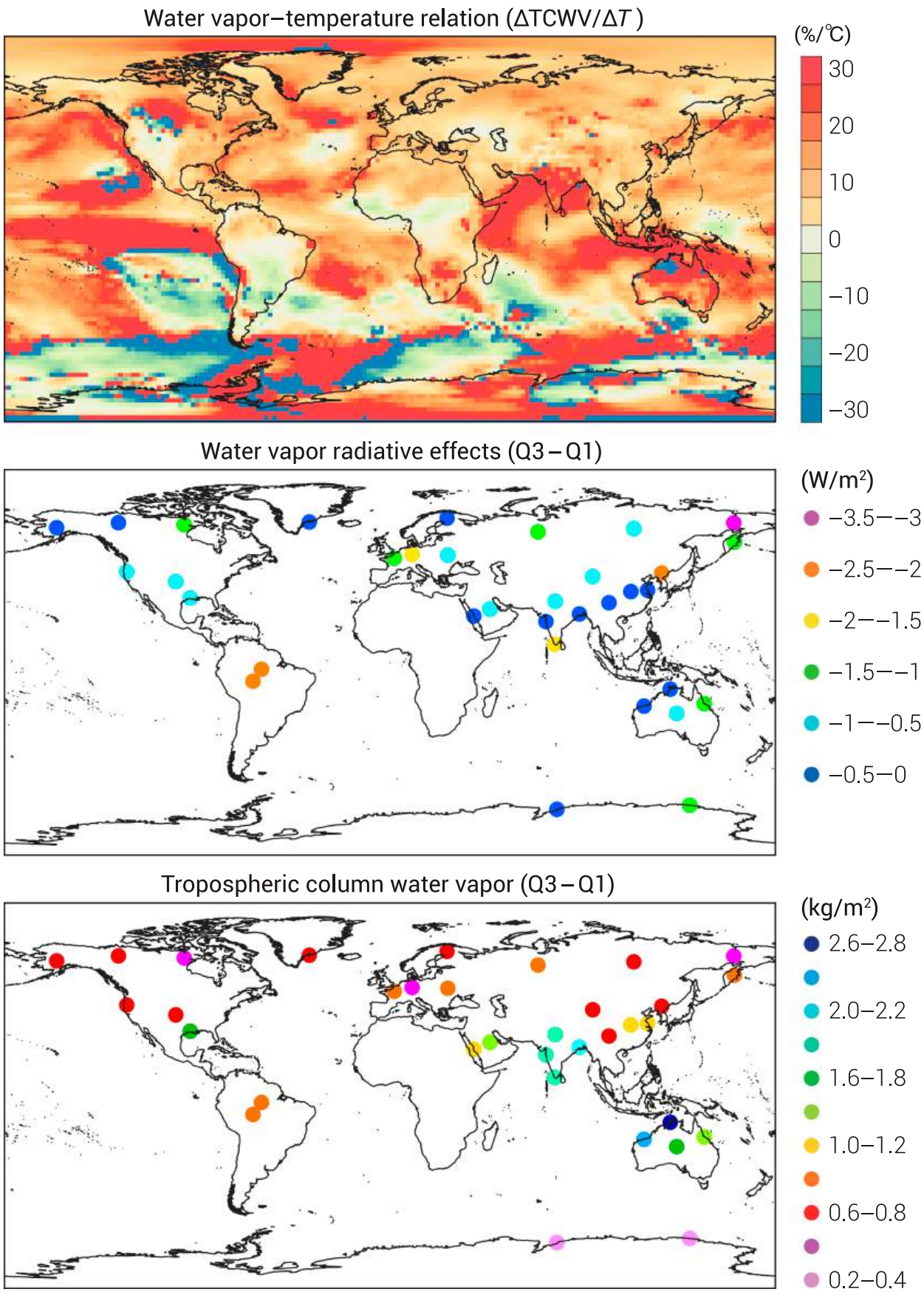

Fig. 7. Top: Water vapor temperature relationship derived from the observations (ΔTCWV/Δ*T*). Middle and bottom: The difference of water vapor radiative effects and tropospheric column water vapor (TCWV), respectively, in the third (Q3) and first (Q1) quartiles at different radiosonde locations.

trends are observed at 600 to 400 hPa, with the lowest values in JJA and highest values in MAM. Regional differences are also observed in the vertical structure of seasonal specific humidity trends. For instance, the trend values are negative (approximately −0.005 g/kg/year) at 800 to 300 hPa over the tropics (in all seasons and annual mean) and 1,000 to 900 hPa in Antarctica, except in DJF. Furthermore, the trends in NML are higher in JJA followed by SON and are within 0.02 g/kg/year. Similarly, trends in SML are higher in DJF, followed by MAM (approximately 0.02 g/kg/year). Irrespective of season, the specific humidity shows significant positive trends throughout the troposphere in the Arctic. These positive trends in the Arctic can be attributed to the rapid warming that leads to more evapotranspiration and, thus, more atmospheric water vapor there. In summary, the vertical structure of specific humidity trends reveals a significant increase in the water vapor throughout the troposphere with notable regional differences.

Trends in sources and drivers of water vapor

Evapotranspiration over land and evaporation from the oceans are the major sources of water vapor, which are driven by surface air temperature and SST, respectively. Studies have shown that water vapor is increasing because of the rise in surface air temperature [7,23,36,37], although moisture transport by winds affects the regional distribution of water vapor. Therefore, we investigate the trends in evapotranspiration, soil moisture, and surface air temperature over land as well as evaporation and SST over oceans, as shown in Fig. 6. The analyses show a consistent rise in air temperature in the northern hemisphere, which is also faster than that of the global average. Similarly, a significant increase in evapotranspiration over land is found during the same period. For example, evapotranspiration is increasing at 0.01 meter water equivalent (mwe)/year over eastern China, parts of India, Brazil, Europe, and some areas in Africa. Rising trends in evapotranspiration in those areas agree with the increasing trend in water vapor in the respective regions. Furthermore, evaporation is increasing in most midlatitude and tropical oceanic regions. For instance, the western and eastern central parts of the Pacific, Atlantic, and Indian Oceans show positive trends in evaporation with values of approximately 0.01 mwe/year. On the other hand, negative trends are estimated in the southern Indian Ocean and west central Pacific Ocean, approximately −0.01 to −0.02 mwe/year. There is heterogeneity in the distribution of trends in water vapor and its sources evapotranspiration and evaporation. Therefore, we also analyze the trends in global water vapor transport (here, with water vapor flux) for the period of 1980—2020 (Fig. S9). We observe that the water vapor flux is increasing significantly over the ocean and land. For instance, a significant rise in water vapor transport is found in the Pacific Ocean (0.5 to 1.5 kg/m/s/year), southern Indian Ocean (approximately 0.5 kg/m/s/year), Atlantic Ocean, Sahara Desert (0.5 kg/m/s/year), Amazonia, and northern United States.

As oceanic evaporation is driven by SST and winds, there are also significant positive trends in SST in global oceanic regions, up to 0.045 °C/year. Positive trends in SST in the Indian and Atlantic Oceans and the eastern and central parts of the Pacific highly agree with the rising water vapor trends there. Similarly, negative trends in SST in the oceanic regions near Antarctica and areas in the western Pacific also match the negative trends of water vapor there. These findings are in accordance with the analyses of Trenberth et al. [36], who demonstrated that the rise in SST drives higher water vapor over oceanic regions.

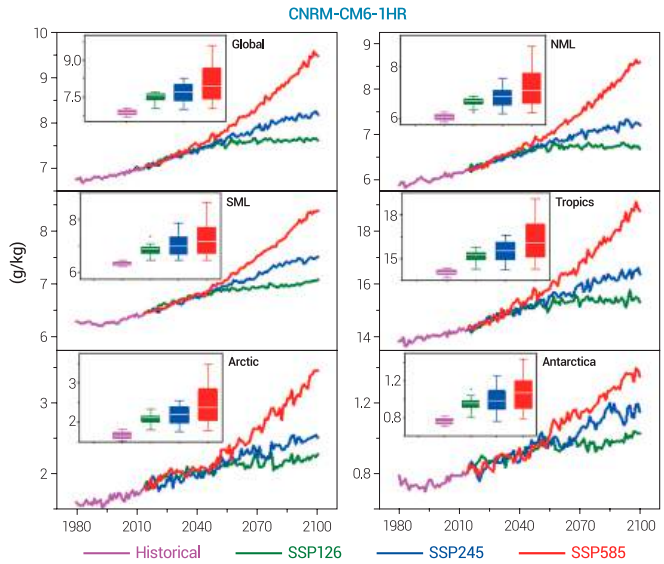

Fig. 8. Projection of water vapor (here, with near-surface specific humidity) under 3 different scenarios SSP126, SSP245, and SSP585 using CMIP6 model CNRM-CM6-1HR for the period 1980–2100. NML and SML indicate northern midlatitudes and southern midlatitudes, respectively.

Furthermore, the negative trend in evaporation estimated in the west central Pacific is consistent with the very high negative trend in water vapor there. Soil moisture is another factor that affects the variability and trends in water vapor. Here, the negative trends in the western part of the United States, eastern part of China, and areas in South America and Europe are consistent with the declining water vapor in those regions. Evaporation from soil also contributes to atmospheric water vapor. As precipitation is a sink of water vapor, a decline in water vapor leads to a decrease in precipitation [38]. Additionally, water vapor is decreasing in the regions of reduced precipitation (Fig. S9). Corresponding to precipitation, soil moisture is also declining, which can lead to browning there. However, there is an inhomogeneity in the distribution of trends in water vapor and precipitation, which can be attributed to other factors, such as prevailing wind conditions, cloud formation, and topography.

WVRE: Implication for global warming

Water vapor and temperature are related to the positive feedback mechanism in the troposphere, where rising temperature leads to an increase in atmospheric water vapor through evaporation and evapotranspiration processes. The increasing water vapor subsequently increases longwave radiation (downward) through the enhanced GHG effect, which, in turn, increases the surface air temperature [39]. For example, every 1 °C rise in temperature increases water vapor by 7% [36]. As both temperature and water vapor show rising trends, we computed changes in water vapor per unit rise in temperature along with the WVRE. In the water vapor temperature relationship, it is observed that water vapor increases per unit rise in temperature, except for some regions in the southern hemisphere, as shown in Fig. 7. For instance, the increase is 20 to 30% in the Indian Ocean, ITCZ, and some regions in the Arctic and Antarctic. Furthermore, the increase in water vapor over global land regions is lower than that over oceans. Nevertheless, the water vapor rise over South America and central Africa is very small, less than 5%.

To examine the changes in radiative effects due to the rise in water vapor, WVRE is estimated for Q3 and Q1 and their difference (Fig. 7). The difference in the Q1 and Q3 WVRE in SW at the surface is higher at Omolong, approximately −3.5 W/m^2. Moderate values of −1.5 to −2.5 W/m^2 are found at Thiruvananthapuram, Porto, Manaus, Meiningen, and Linjiang. However, the smallest difference is observed at stations in India, China, the Arctic, and Antarctica, consistent with the quartile difference in water vapor there. Similarly, at the stations where the WVRE difference is higher, water vapor is also high, except at some stations. There are regional differences in WVRE changes corresponding to water vapor, indicating the impact of regional atmospheric and climate processes. We have also shown the WVRE at the Q1 and Q3 separately (Fig. S10). The Q3 WVRE is higher than Q1, consistent with the quartile difference in water vapor. We find the highest amount of WVRE at Manaus (−63.25 W/m^2 [Q1]; −65.26 W/m^2 [Q3]) and Porto (−64.25 W/m^2 [Q1]; −66.27 W/m^2), matching the high amount of water vapor at the respective stations. However, the smallest WVRE is observed in both polar regions because of the lower amount of water vapor there. The higher values of WVRE in Q3 clearly indicate that the rise in water vapor leads to higher WVRE and, thus, enhanced surface temperature. Similar results are also observed by Salamalikis et al. [40], albeit with differences in the WVRE values due to the difference in temporal coverage and quartile computation. As discussed, because higher water vapor increases temperature, we also analyze the future projection of water vapor.

Future projection of water vapor

Compared to the historical projection (reference data; 1980–2015), the future projection (up to 2100) of water vapor (here with near-surface specific humidity) using the CMIP6 model CNRM-CM6-1HR under 3 different scenarios is illustrated in Fig. 8. We average the water vapor values over the globe, NML, SML, tropics, Arctic, and Antarctica for all 3 scenarios. It is expected that the amount of water vapor in all regions will increase in all 3 scenarios, and the change under SSP585 is higher than that under SSP245 and SSP126. Among the regions, the rise in water vapor over the Arctic (3.46 g/kg) and Antarctica (1.35 g/kg) is very high under SSP585, approximately twice the historical mean [1.66 g/kg for the Arctic and 0.76 g/kg for Antarctica]. Because polar regions are susceptible to increases in temperature, water vapor is expected to increase in the future, as shown by the projections [41]. Tropics with high temperatures and massive evaporation show an unprecedented rise in water vapor under SSP585 (18.74 g/kg) at the end of the 21st century compared to the historical value (14.07 g/kg). However, the low-emission scenario SSP126 shows a very small change since 2050, approximately 14.95 to 15.78 g/kg. A similar pattern is also observed in the global average and NML under SSP126, where water vapor is nearly constant since 2050, but a notable rise is observed under SSP585 and SSP245.

We also compared the results with another CIMP6 model projection, CIESM, and found that growth in future water vapor is very high under SSP585 relative to other scenarios, as simulated by the CNRM-CM6-1HR model (Fig. S11). Additionally, the distribution of water vapor under the low-emission scenarios is similar to that of CNRM-CM6-1HR for all regions, but the values are slightly higher. Briefly, the CMIP6 models reveal that water vapor is increasing, with a significant surge in both polar regions, approximately twice the historical mean. Therefore, an increase in water vapor in the future would increase the temperature and, thus, affect the regional and global climate.

Conclusion

This study investigates the long-term (1980–2020) changes in global tropospheric water vapor. The annual mean tropospheric water vapor ranges from 5 to 60 kg/m^2, with greater variability over oceans than over land. There is clear seasonal variability, where the amount of water vapor is highest in summer and lowest in winter, except in the tropics. Water vapor variability in the tropics is strongly affected by ENSO and PDO. Similarly, water vapor variability in the southern and northern hemispheres is affected by SHSIE and NHSIE, respectively. There is also a notable increase in global tropospheric water vapor (0.025 to 0.1 kg/m^2/year and at 1,000 to 700 hPa with 0.001 to 0.015 g/kg/year). In addition, regardless of season, a notable rise in tropospheric water vapor and a rise in specific humidity throughout the troposphere are observed in the Arctic because of the anomalous rise in temperature in the region, the Arctic amplification. Considering that water vapor is the most abundant GHG and is rising globally, it would increase regional and global temperatures through radiative effects, approximately −5 to −70 W/m^2 at the surface, depending on the region. The rise in temperature would also lead to an increase in evapotranspiration, which would eventually result in an increase in the amount of atmospheric water vapor because of its positive feedback mechanism. Water vapor is expected to increase significantly by the end of the 21st century, with high values in the polar regions, approximately twice the historical or current values. Furthermore, an increase in atmospheric water vapor amplifies the warming caused by other GHGs, which would further amplify global warming and adversely affect the global and regional climate. Therefore, this study provides new evidence of global change associated with the increase in global water vapor.

Acknowledgments

We thank the director of the Indian Institute of Technology Kharagpur (IIT Kgp), the chairman of CORAL IIT Kgp, and the Ministry of Education (MoE) for making this study possible. V.K.P. thanks MoE and IIT KGP for assistance. For MERRA 2 and AIRS data, we also wish to thank the NASA GES DISC for creating and maintaining Giovanni's online data system. **Funding:** This study received no funding. **Author contributions:** V.K.P.: Conceptualization, methodology, data analysis, visualization, and writing—original draft. J.K.: Conceptualization, methodology, visualization, supervision, and review and editing of the original draft. **Competing interests:** The authors declare that they have no competing interests.

Data Availability

Data can be found in the following: ER5 data: https://cds.climate.copernicus.eu/cdsapp#!/dataset/reanalysis-era5-single-levels-monthly-means?tab=overview; MERRA 2 and AIRS data: https://giovanni.gsfc.nasa.gov/giovanni/; GLDAS data: https://disc.gsfc.nasa.gov/datasets/GLDAS_NOAH025_M_2.1/

summary; CRU: https://crudata.uea.ac.uk/cru/data/hrg/; NOAA CPC: https://psl.noaa.gov/data/climateindices/list/; and IGRA v02: https://www.ncei.noaa.gov/access/metadata/landing-page/bin/iso?id=gov.noaa.ncdc:C00975.

Supplementary Materials

Figs. S1 to S11
Tables S1 to S3

References

1. Sherwood SC, Roca R, Weckwerth TM, Andronova NG. Tropospheric water vapor, convection, and climate. *Rev Geophys*. 2010;48(2):RG2001.
2. Wagner T, Beirle S, Grzegorski M, Platt U. Global trends (1996–2003) of total column precipitable water observed by global ozone monitoring experiment (GOME) on ERS-2 and their relation to near-surface temperature. *J Geophys Res*. 2006;111(D12).
3. Dessler AE, Sherwood SC. Atmospheric science: A matter of humidity. *Science*. 2009;323(5917):1020–1021.
4. Wang JXL, Gaffen DJ. Late-twentieth-century climatology and trends of surface humidity and temperature in China. *J Clim*. 2001;14:2833–2845.
5. Soden BJ, Jackson DL, Ramaswamy V, Schwarzkopf D, Huang X. The radiative signature upper tropospheric moistening. *Science*. 2005;310:841–844.
6. Santer BD, Wigley TML, Gleckler PJ, Bonfils C, Wehner MF, AchutaRao K, Barnett TP, Boyle JS, Brüggemann W, Fiorino M, et al. Forced and unforced ocean temperature changes in Atlantic and Pacific tropical cyclogenesis regions. *Proc Natl Acad Sci*. 2006;103(38):905–910.
7. Dai A. Recent climatology, variability and trends in global surface humidity. *J Clim*. 2006;19:3589–3606.
8. Held IM, Soden BJ. Robust responses of the hydrological cycle to global warming. *J Clim*. 2006;19(21):5686–5699.
9. Hansen J, Lacis A, Rind D, Russell G, Stone P, Fung I, Ruedy R, Lerner J. Climate sensitivity: Analysis of feedback mechanisms. *Geophys Monogr*. 1984;29:130–163.
10. Zhang X, Zwiers FW, Hegerl GC, Lambert FH, Gillett NP, Solomon S, Stott PA, Nozawa T. Detection of human influence on twentieth-century precipitation trends. *Nature*. 2007;448:461–465.
11. Allan RP, Soden BJ. Atmospheric warming and the amplification of precipitation extremes. *Science*. 2008;2008(321):1481–1484.
12. Willett KM, Gillett NP, Jones PD, Thorne PW. Attribution of observed surface humidity changes to human influence. *Nature*. 2007;449:710–712.
13. Ross RJ, Elliott WP. Radiosonde-based northern hemisphere tropospheric water vapour trends. *J Clim*. 2001;14:1602–1611.
14. Bengtsson L, Hagemann S, Hodges KI. Can climate trends be calculated from reanalysis data. *J Geophys Res Atmos*. 2004;109:D11.
15. Mieruch S, Noël S, Bovensmann H, Burrows JP. Analysis of global water vapour trends from satellite measurements in the visible spectral range. *Atmos Chem Phys*. 2008;8:491–504.
16. Bony S, Stevens B, Frierson DM, Jakob C, Kageyama M, Pincus R, Shepherd TG, Sherwood SC, Siebesma AP, Sobel AH, et al. Clouds, circulation and climate sensitivity. *Nat Geosci*. 2015;8(4):261–268.
17. Hall A, Manabe S. The role of water vapor feedback in unperturbed climate variability and global warming. *J Clim*. 1999;12(8):2327–2346.
18. Held IM, Soden BJ. Water vapor feedback and global warming. *Annu Rev Energy Environ*. 2000;25(1):441–475.
19. Hersbach H, Bell B, Berrisford P, Hirahara S, Horányi A, Muñoz-Sabater J, Nicolas J, Peubey C, Radu R, Schepers D, et al. The ERA5 global reanalysis. *Q J R Meteorol Soc*. 2020;146(730):1999–2049.
20. Dessler A, Zhang Z, Yang P. Water-vapor climate feedback inferred from climate fluctuations, 2003–2008. *Geophys Res Lett*. 2008;35(20):L20704.
21. Pierce DW, Barnett TP, Fetzer EJ, Gleckler PJ. Three-dimensional tropospheric water vapor in coupled climate models compared with observations from the AIRS satellite system. *Geophys Res Lett*. 2006;33(21):L21701.
22. Durre I, Yin X, Vose RS, Applequist SJ, Arnfield J. Enhancing the data coverage in the integrated global radiosonde archive. *J Atmos Ocean Technol*. 2018;35(9):1753–1770.
23. Patel VK, Kuttippurath J. Significant increase in water vapour over India and Indian Ocean: Implications for tropospheric warming and regional climate forcing. *Sci Total Environ*. 2022;838:Article 155885.
24. Rama Varma Raja MK, Gutman SI, Yoe JG, McMillin LM, Zhao J. The validation of AIRS retrievals of integrated precipitable water vapor using measurements from a network of ground-based GPS receivers over the contiguous United States. *J Atmos Ocean Technol*. 2008;25(3):416–428.
25. Hearty TJ, Savtchenko A, Tian B, Fetzer E, Yung YL, Theobald M, Vollmer B, Fishbein E, Won YI. Estimating sampling biases and measurement uncertainties of AIRS/AMSU-A temperature and water vapor observations using MERRA reanalysis. *J Geophys Res Atmos*. 2014;119(6):2725–2741.
26. Silva FN, Vega-Oliveros DA, Yan X, Flammini A, Menczer F, Radicchi F, Kravitz B, Fortunato S. Detecting climate teleconnections with granger causality. *Geophys Res Lett*. 2021;48(18):Article e2021GL094707.
27. Ricchiazzi P, Yang S, Gautier C, Sowle D. SBDART: A research and teaching software tool for plane-parallel radiative transfer in the Earth's atmosphere. *Bull Am Meteorol Soc*. 1998;79(10):2101–2114.
28. Vaquero-Martínez J, Antón M, Ortiz de Galisteo JP, Román R, Cachorro VE. Water vapor radiative effects on short-wave radiation in Spain. *Atmos Res*. 2018;205:18–25.
29. Trenberth KE, Smith L. The mass of the atmosphere: A constraint on global analyses. *J Clim*. 2005;18(6):864–875.
30. Soden BJ, Wetherald RT, Stenchikov GL, Robock A. Global cooling after the eruption of mount Pinatubo: A test of climate feedback by water vapor. *Science*. 2002;296(5568):727–730.
31. Allan RP, Willett KM, John VO, Trent T. Global changes in water vapor 1979–2020. *J Geophys Res Atmos*. 2022;127(12):Article e2022JD036728.
32. Power S, Casey T, Folland C, Colman A, Mehta V. Inter-decadal modulation of the impact of ENSO on Australia. *Clim Dyn*. 1999;15:319–324.
33. Rinke A, Dethloff K, Dorn W, Handorf D, Moore JC. Simulated Arctic atmospheric feedbacks associated with late summer sea ice anomalies. *J Geophys Res Atmos*. 2013;118(14):7698–7714.
34. Zhang L, Wu L, Gan B. Modes and mechanisms of global water vapor variability over the twentieth century. *J Clim*. 2013;26(15):5578–5593.

35. Kopec BG, Feng X, Michel FA, Posmentier ES. Influence of sea ice on Arctic precipitation. *Proc Natl Acad Sci U S A*. 2016;113(1):46–51.
36. Trenberth KE, Fasullo J, Smith L. Trends and variability in column-integrated atmospheric water vapour. *Clim Dyn*. 2005;24:741–758.
37. Lu N, Qin J, Gao Y, Yang K, Trenberth KE, Gehne M, Zhu Y. Trends and variability in atmospheric precipitable water over the Tibetan plateau for 2000–2010. *Int J Climatol*. 2015;35(7):1394–1404.
38. Wong S, Fetzer EJ, Tian B, Lambrigtsen B, Ye H. The apparent water vapor sinks and heat sources associated with the intraseasonal oscillation of the Indian summer monsoon. *J Clim*. 2011;24(16):4466–4479.
39. Ghatak D, Miller J. Implications for Arctic amplification of changes in the strength of the water vapor feedback. *J Geophys Res Atmos*. 2013;118(14):7569–7578.
40. Salamalikis V, Vamvakas I, Gueymard CA, Kazantzidis A, Kazantzidis A. Atmospheric water vapor radiative effects on shortwave radiation under clear skies: A global spatiotemporal analysis. *Atmos Res*. 2021;251:Article 105418.
41. Overland J, Dunlea E, Box JE, Corell R, Forsius M, Kattsov V, Olsen MS, Pawlak J, Reiersen L, Wang M. The urgency of Arctic change. *Pol Sci*. 2019;21:6–13.